



Sensitivity Reach of Gamma-Ray Measurements for Strong Cosmological Magnetic Fields

Alexander Korochkin^{1,2,4}, Oleg Kalashev^{1,3,4}, Andrii Neronov^{2,5} , and Dmitri Semikoz²

¹INR RAS, 60 October anniversary prosp. 7a, Moscow, Russia

²Université de Paris, CNRS, Astroparticule et Cosmologie, F-75013 Paris, France

³Moscow Institute for Physics and Technology, 9 Institutskiy per., Dolgoprudny, Moscow Region, 141701 Russia

⁴Novosibirsk State University, Pirogova 2, Novosibirsk, 630090 Russia

⁵Astronomy Department, University of Geneva, Ch. d'Ecogia 16, 1290, Versoix, Switzerland

Received 2020 August 27; revised 2020 October 29; accepted 2020 October 29; published 2021 January 14

Abstract

A primordial magnetic field with strength in the 1–10 pG range can resolve the tension between different measurements of the Hubble constant and provide an explanation for the excess opacity in the 21 cm line at redshift $15 < z < 20$ if it is present during the recombination and reionization epochs. This field can also survive in the voids of the large-scale structure in the present day universe. We study the sensitivity reach of the gamma-ray technique for measurement of such a relatively strong cosmological magnetic field using deep exposure(s) of the nearest hard spectrum blazar(s) with CTA telescopes. We show that the gamma-ray measurement method can sense the primordial magnetic field with a strength of up to 10^{-11} G. Combination of the cosmic microwave background and gamma-ray constraints can thus sense the full range of possible cosmological magnetic fields to confirm or rule out their relevance to the problem of the origin of cosmic magnetic fields, as well as their influence on recombination and reionization epochs.

Unified Astronomy Thesaurus concepts: [Extragalactic magnetic fields \(507\)](#); [Blazars \(164\)](#)

1. Introduction

Magnetic fields are present in almost every observable astronomical object. Yet their existence and role in the early universe is uncertain. A combination of γ -ray lower bounds (Neronov & Vovk 2010; Ackermann et al. 2018) and radio and cosmic microwave background (CMB) upper bounds (Kronberg 1994; Planck Collaboration 2016) on the intergalactic magnetic field (IGMF) provides evidence for the existence of fields with strengths of 10^{-16} G $< B < 10^{-9}$ G in the intergalactic medium (see Figure 1 for a summary of known constraints on IGMF, summarized by Neronov & Semikoz 2009; Durrer & Neronov 2013). However, the primordial nature of these fields has yet to be established.

Jedamzik & Pogosian (2020) have recently shown that accounting for the magnetic field driven turbulence on plasma at the epoch of recombination modifies the estimate of the Hubble parameter from the CMB data and relaxes the 4.4 σ tension between Planck measurements $H_0 = 67.36 \pm 0.54$ km (s Mpc)⁻¹ based on $z \simeq 10^3$ data (Planck Collaboration 2018) and present day universe measurements $H_0 = 74.03 \pm 1.42$ km (s Mpc)⁻¹ using supernovae Type Ia (Riess et al. 2019) and $H_0 = 73.3_{-1.8}^{+1.7}$ km (s Mpc)⁻¹ based on gravitationally lensed systems (Wong et al. 2020). The reasoning of Jedamzik & Pogosian (2020) further develops the argument of Jedamzik & Saveliev (2019) that a magnetic field present at the epoch of recombination induces clumping of baryonic matter and in this way modifies the recombination process. Jedamzik & Saveliev (2019) have used this argument to derive a strong upper bound $B \lesssim 10^{-11}$ G at the epoch of recombination. This bound is shown by the black arrow in Figure 1. The cosmological magnetic field with the strength of $\sim 10^{-11}$ G is expected to have a correlation length of about $\lambda_B \simeq 1[B/10^{-11} \text{ G}]$ kpc, which is the largest processed eddy size at the epoch of recombination (Banerjee & Jedamzik 2004).

Another indication of the existence of cosmological magnetic fields can be derived from measurements of redshift dependent absorption by the 21 cm line of neutral hydrogen at redshifts of about $z \sim 10$. The EDGES experiment has recently reported an excess opacity of the universe in the redshift range of $15 < z < 20$ (Bowman et al. 2018). This indicates that an efficient cooling mechanism of baryonic matter is operating during this epoch. Interaction of matter with magnetic field can provide both cooling (via pumping of thermal energy into magnetic field) and heating (via decay of MHD turbulence) of baryonic matter. It is possible to interpret the EDGES observation in terms of cooling through the interaction with magnetic fields (Natwariya & Bhatt 2020). The magnetic field strength, which is required to explain EDGES data, is comparable to that needed to resolve the Hubble parameter measurement tension, 5×10^{-13} G $< B < 6 \times 10^{-12}$ G (Natwariya & Bhatt 2020).

The magnetic fields surviving until the epochs of recombination and reionization should have been produced during phase transitions in the early universe (see Durrer & Neronov 2013 for a review). The presence of a helical magnetic field at the epoch of the electroweak phase transition can enable an explanation of the baryon asymmetry of the universe within the standard model of particle physics (Giovannini & Shaposhnikov 1998; Fujita & Kamada 2016). The range of magnetic field strength 10^{-14} G $< B < 10^{-12}$ G, which is compatible with this baryogenesis scenario is shown by the green shading in Figure 1. Remarkably, the field strength required for a successful explanation of the baryon asymmetry is consistent with that needed for an explanation of the EDGES signal and of the Hubble parameter measurement tensions.

The combination of these observational hints for the existence of a cosmological magnetic field defines an order-of-magnitude wide “sweet spot” around $B \sim 10^{-12}$ G in which the field estimates from multiple effects intersect. The most

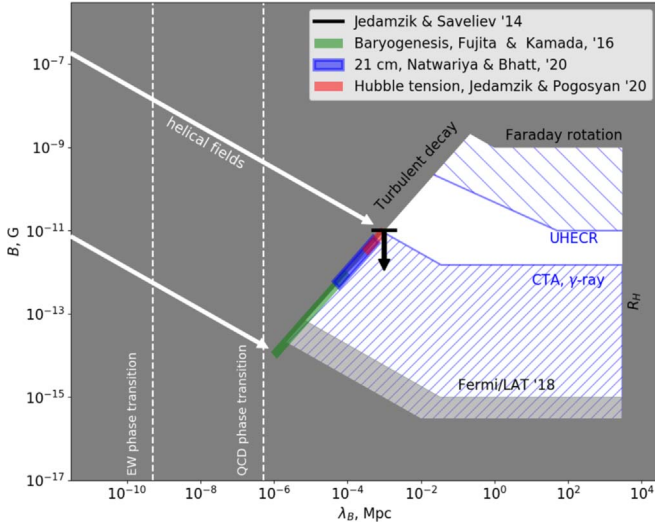


Figure 1. Known constraints on the strength and correlation length of the IGMF (Neronov & Semikoz 2009; Durrer & Neronov 2013). Red, blue, and green lines show hints of the existence of a cosmological magnetic field from the CMB (Jedamzik & Pogossyan 2020), 21 cm line (Natwariya & Bhatt 2020), and baryogenesis (Fujita & Kamada 2016) correspondingly. Blue dashed regions show the sensitivity of different detection techniques (Neronov & Semikoz 2009; Durrer & Neronov 2013). Black upper bound is from the analysis of the CMB signal by Jedamzik & Saveliev (2019).

convincing evidence for the existence of a field with such strength would be its direct detection in the intergalactic medium. In what follows we explore the possibility of the measurement of such a field with γ -ray telescopes. We demonstrate that even though the field is at the upper sensitivity end of the γ -ray technique, its detection should still be possible with a deep exposure of the nearest blazars with CTA.

2. Analytical Estimates

Fields with strengths in the range of $B \sim 10^{-12}$ G are at the upper end of the sensitivity reach of the γ -ray measurement method (Neronov & Semikoz 2009). They are strong enough to deflect trajectories of electrons with energies in the 10–100 TeV range. This implies that the highest energy γ -ray signal accessible to telescopes should be used for the signal measurements. In this situation it is not clear if the small angle deflection approximation previously used for the sensitivity estimates used by Neronov & Semikoz (2009) is valid. We reassess the analytical estimates in this high-energy/strong field regime below.

The correlation length λ_B of cosmological magnetic field scales with the strength as (Banerjee & Jedamzik 2004)

$$B \sim 10^{-11} \left[\frac{\lambda_B}{1 \text{ kpc}} \right] \text{G}. \quad (1)$$

The field power spectrum is shaped by the turbulence on scales shorter than λ_B . The integral length scale of the field with power spectrum $P_B(k) \propto k^{-n}$ is

$$\lambda_B \approx L_B \frac{n-1}{2n} = \frac{L_B}{5} \quad (2)$$

for $n = 5/3$ (assuming the Kolmogorov turbulence spectrum), where L_B is the maximum scale of the Kolmogorov spectrum.

We consider secondary emission induced by interactions of primary γ -rays with energies $E_{\gamma 0}$. The mean free path of these

γ -rays through the EBL is

$$\lambda_{\gamma 0} \simeq 2.5 \left[\frac{E_{\gamma 0}}{100 \text{ TeV}} \right]^{-1.6} \text{Mpc}. \quad (3)$$

For the analytical estimates we assume that each primary γ -ray produces an electron and a positron with energies of $E_e = E_{\gamma 0}/2$. The electrons and positrons cool due to the inverse Compton scattering of CMB photons on the distance scale

$$D_e \simeq 7 \left[\frac{E_e}{50 \text{ TeV}} \right]^{-1} \text{kpc} \quad (4)$$

in the Thomson regime of inverse Compton scattering⁶ relevant for the scattering of CMB photons by electrons with energies $\lesssim 100$ TeV. Such electrons produce inverse Compton emission at the energy

$$E_\gamma \simeq 8 \left[\frac{E_e}{50 \text{ TeV}} \right]^2 \text{TeV}. \quad (5)$$

The gyroradius of electrons is

$$R_L \simeq 5 \left[\frac{E_e}{50 \text{ TeV}} \right] \left[\frac{B}{10^{-11} \text{ G}} \right]^{-1} \text{kpc}. \quad (6)$$

Electrons are typically deflected by an angle of

$$\delta = \frac{\lambda_B}{R_L} \simeq 0.06 \left[\frac{E_e}{50 \text{ TeV}} \right]^{-1} \left[\frac{B}{10^{-11} \text{ G}} \right]^2 \quad (7)$$

on the distance scale about the integral length of the magnetic field (we have used the scaling $B \propto \lambda_B$ suggested by Equations (1) and (2)). Accumulation of such small deflections on the electron cooling distance scale D_e results in the overall deflection

$$\begin{aligned} \Delta &= \sqrt{\frac{D_e}{\lambda_B}} \delta \simeq 0.2 \left[\frac{E_e}{50 \text{ TeV}} \right]^{-3/2} \left[\frac{B}{10^{-11} \text{ G}} \right]^{3/2} \\ &\simeq 0.2 \left[\frac{E_\gamma}{8 \text{ TeV}} \right]^{-3/4} \left[\frac{B}{10^{-11} \text{ G}} \right]^{3/2}. \end{aligned} \quad (8)$$

If the field strength is $B \sim 10^{-11}$ G, the opening angle of the secondary emission cone at 2 TeV can be as large as the opening angle of the AGN jets. The secondary emission flux within the cone gets suppressed as

$$\begin{aligned} \frac{F_{\text{ext}}}{F_{\gamma 0}} &= \frac{\Theta_{\text{jet}}^2}{\Delta^2} \simeq 1 \left[\frac{E_\gamma}{8 \text{ TeV}} \right]^{3/2} \\ &\left[\frac{B}{10^{-11} \text{ G}} \right]^{-3} \left[\frac{\Theta_{\text{jet}}}{10^\circ} \right]^2, \quad B \gtrsim 10^{-11} \text{ G}, \end{aligned} \quad (9)$$

where we have assumed $\Theta_{\text{jet}} \sim 10^\circ \simeq 0.2$. Such flux suppression occurs below the energy at which $\Delta = \Theta_{\text{jet}}$,

$$E_{\text{crit}} = 8 \left[\frac{B}{10^{-11} \text{ G}} \right]^2 \left[\frac{\Theta_{\text{jet}}}{10^\circ} \right]^{4/3} \text{TeV}. \quad (10)$$

⁶ Our numerical modeling takes into account the full Klein–Nishina cross-section of inverse Compton scattering. The Klein–Nishina effect corrects analytical estimates, but does not change the qualitative picture presented in this section.

If $B < 10^{-11}$ G, the deflection angle Δ is smaller than the opening angle of the jet and extended emission is still observable toward 10 TeV energy.

The maximal possible angular size of the extended emission is determined by the transverse size of the jet at the distance $\lambda_{\gamma 0}$

$$R_{\text{ext,max}} = \Theta_{\text{jet}} \lambda_{\gamma 0} \simeq 0.5 \left[\frac{\Theta_{\text{jet}}}{10^\circ} \right] \left[\frac{E_{\gamma 0}}{100 \text{ TeV}} \right]^{-1.6} \text{ Mpc}. \quad (11)$$

This corresponds to the angular size

$$\Theta_{\text{ext,max}} = \frac{R_{\text{ext}}}{D} \simeq 0.24 \left[\frac{\Theta_{\text{jet}}}{10^\circ} \right] \left[\frac{E_{\gamma 0}}{100 \text{ TeV}} \right]^{-1.6} \left[\frac{D}{120 \text{ Mpc}} \right]^{-1} \simeq 0.24 \left[\frac{\Theta_{\text{jet}}}{10^\circ} \right] \left[\frac{E_{\gamma}}{8 \text{ TeV}} \right]^{-0.8} \left[\frac{D}{120 \text{ Mpc}} \right]^{-1}, \quad (12)$$

where we have used the distances to Mrk 421 and Mrk 501 for the numerical estimate. The time delay of the extended signal can be estimated as

$$T_{\text{ext,max}} = D \Theta_{\text{ext,max}}^2 / c \simeq 8 \left[\frac{\Theta_{\text{jet}}}{10^\circ} \right]^2 \left[\frac{E_{\gamma}}{8 \text{ TeV}} \right]^{-1.6} \text{ kyr}. \quad (13)$$

This timescale imposes a requirement on the duty cycle of the source for which the extended emission is detectable: the source should have been active over the last 10 kyr, which is plausible given the fact that the source possesses a kiloparsec-scale jet (Giroletti et al. 2008).

Note that the maximal extended source size does not depend on the magnetic field strength. Instead, it is the extended source flux that scales with magnetic field. However, this dependence could hardly be used for the estimation of the field strength because of uncertainty of the opening angle of the jet and because of the very rapid decline of the extended source flux with the field strength. Because of this limitation, we choose to show in Figure 1 the lower bound for the Fermi/LAT telescope derived in the regime of small deflection angles of electrons (see Ackermann et al. 2018 for details).

3. Selection of Best Target for the Search of Strong IGMF

Probe of the strongest fields $B \lesssim 10^{-11}$ G requires

- large primary point-source power in the 100 TeV energy range,
- detectability of extended emission in multi-TeV energy range, and
- presence of primordial IGMF in the several Mpc region around the source.

Below we present arguments that at least one source, Mrk 501, fulfills these three conditions and can be used for the probe of strong IGMF of cosmological origin.

3.1. Are There 100 TeV Bright Blazars?

There are currently no measurements or estimates of the blazar luminosities at 100 TeV. The highest energy photons detected from blazars are those from the two nearest BL Lac objects, Mrk 421 and Mrk 501. Figure 2 shows the spectral energy distribution of these sources measured by HAWC (Coutiño de Leon et al. 2019). One can see that even though

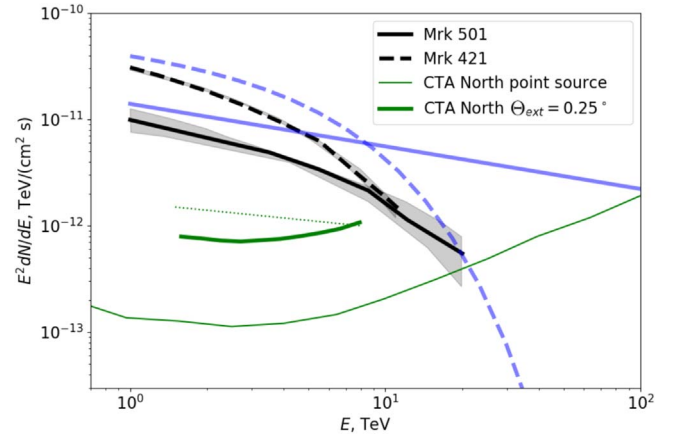


Figure 2. Comparison of high-energy ends of the spectra of Mrk 421 and Mrk 501 (Coutiño de Leon et al. 2019). Black curves are observed, and blue curves are the intrinsic spectra of the sources. Thin and thick green lines show CTA North sensitivity to point sources and to the extended sources with angular size $\theta = 0.25^\circ$ (<https://www.cta-observatory.org/science/cta-performance/>). Green dotted line shows an analytical estimate of the secondary γ -ray flux from Mrk 501 in the 1–10 energy range assuming no influence of IGMF.

Mrk 421 is the brightest source at TeV, it has a softer spectrum and its intrinsic luminosity is most probably strongly suppressed at 100 TeV. To the contrary, Mrk 501 has a harder spectrum that does not show any signature of high-energy cutoff. The spectrum is measured up to 20 TeV. In view of this fact, we consider Mrk 501 as a more promising candidate for the search of the strongest IGMF and the following calculations are limited to this source. We assume that its intrinsic spectrum extends up to 100 TeV, as shown in Figure 2.

Extrapolating the power law measured by HAWC up to 100 TeV, we find that the intrinsic flux of the source at this energy should be at the level of

$$F_{\gamma 0}(100 \text{ TeV}) \simeq (2.5 \pm 1) \times 10^{-12} \text{ TeV}/(\text{cm}^2 \text{ s}). \quad (14)$$

3.2. Detectability of Multi-TeV Extended Emission

Most of the intrinsic flux in the 100 TeV energy range is absorbed in the intergalactic medium and is converted to the extended emission. In the regime $B < 10^{-11}$ G, the extended emission flux is not suppressed by the widening of the opening angle of the emission cone and one can expect that the flux of the extended source is

$$F_{\text{ext}}(8 \text{ TeV}) \sim F_{\gamma 0}(100 \text{ TeV})/2 \sim 10^{-12} \text{ TeV}/(\text{cm}^2 \text{ s}). \quad (15)$$

This flux level is well above the CTA point-source sensitivity, shown by the lowermost green solid curve in Figure 2. The sensitivity limit $F_{\text{CTA,ps}} \simeq 5 \times 10^{-14} \text{ TeV cm}^2 \text{ s}^{-1}$ in the 1–10 TeV range is determined by the statistical fluctuations of the background within the point-spread function $\Theta_{\text{psf}} \simeq 0.04^\circ$.⁷ The sensitivity for extended source flux worsens with the increase of the source size, roughly as

$$F_{\text{CTA,ext}} = F_{\text{CTA,ps}} \frac{\Theta_{\text{ext}}}{\Theta_{\text{PSF}}} \simeq 3 \times 10^{-13} \left[\frac{\Theta_{\text{ext}}}{0.25^\circ} \right] \text{ TeV}/(\text{cm}^2 \text{ s}). \quad (16)$$

⁷ <https://www.cta-observatory.org/science/cta-performance/>

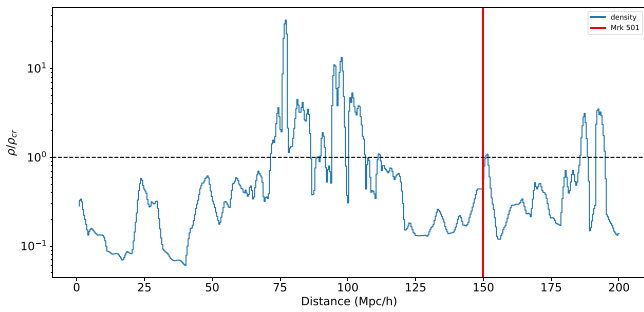


Figure 3. Dark matter density profile along the line of sight toward Mrk 501 based on constrained simulations of the LSS (Jasche & Lavaux 2019).

This sensitivity is compared with the expected extended source flux in Figure 2. As one can see, the extended flux is above the sensitivity limit and might be detectable. However, the extended emission appears on top of the point-source flux and more detailed analysis is required for verification of its detectability.

3.3. IGMF in the Direction of Mrk 501

The γ -ray measurement method is sensitive to the weakest volume filling IGMF along the line of sight toward the source. This field is typically found in the voids of the LSS. TeV γ -rays can cross many voids before being absorbed in pair production. This is not the case for the 100 TeV γ -rays, which can potentially be used to probe the strongest IGMF $B \sim 10^{-11}$ G. These γ -rays can only probe the field within several megaparsecs around the source. Indeed, in this case the effect of extended emission is most significant at energies of secondary photons in the range of ~ 2 –10 TeV. The corresponding energy of primary photons is about 50–100 TeV. Considering the standard EBL models the typical mean free path of such photons is 3–10 Mpc. If the source is occasionally found in or near a large galaxy cluster, or the line of sight points toward a filament of the LSS, the field strength can be much higher than the typical void field making the line of reasoning described above inapplicable.

To explore environmental effects around Mrk 501, we rely on constrained cosmological simulations derived using the Bayesian Origin Reconstruction from Galaxies (BORG) inference method (Jasche & Wandelt 2013). BORG provides a statistical ensemble of initial conditions that all match detailed observations of galaxy count in the universe. To achieve this, it relies on modeling the evolution of large-scale structures starting from high redshift using a dynamical model. Then the probability of such a sample is compared volume element by volume element to data from a galaxy survey assuming some bias function and Poisson statistics for the number count (Jasche & Wandelt 2013). The initial conditions can then be resimulated with software of the user’s choice. For the data considered here, the dynamical model is a particle mesh N -body solver with 20 timesteps; the data are provided by the 2M++ galaxy compilation (Lavaux & Hudson 2011). The resolution of the density contrast of the initial conditions and at $z = 0$ are set to $2.64h^{-1}$ Mpc. The details of the algorithm and of the inference procedure are provided in Jasche & Lavaux (2019).

Using the dark matter density as an estimator of the strength of magnetic field we found (see Figure 3) that the IGMF around the source does not appear in the reach galaxy cluster. Instead

there is a large void just next to the Mrk 501 with the average density ρ below the critical density of the universe and there the magnetic field is not amplified in the course of structure formation. Numerical modeling of the IllustrisTNG simulation (Marinacci et al. 2018) shows that such amplification only occurs in the regions with overdensity $\rho/\rho_{cr} \gtrsim 10$.

4. Numerical Modeling

Qualitative arguments presented in the previous section show that even if the IGMF of cosmological origin is as strong as $B \sim 10^{-11}$ G, it should still be possible to detect it via the search of extended emission around Mrk 501, which is the brightest blazar in the 10 TeV sky.

In this section we support this qualitative argument with numerical modeling of the extended source signal. For this purpose we use the Monte Carlo simulation code developed in Berezhinsky & Kalashev (2016), which was also tested by comparison with the alternative cascade simulations (Taylor et al. 2011; Kachelriess et al. 2012; Kalashev & Kido 2015).

We consider a primary γ -ray source with the power-law spectrum with the slope $dN/dE \propto E^{-2.4}$ extending up to 100 TeV energy, situated at the distance of $D = 150$ Mpc. The γ -rays are emitted into a jet with opening angle $\Theta_{jet} = 5^\circ$ aligned along the line of sight.

We propagate the primary γ -ray beam toward the observer, taking into account pair production on extragalactic background light (EBL). The EBL spectrum is that of Gilmore et al. (2012). Electrons and positrons produced by absorbed γ -rays lose energy due to inverse Compton scattering on EBL and CMB. The IGMF present that deflects electrons and positrons is assumed to have strength and correlation length satisfying the relation (1).

The field is generated with the Kolmogorov power spectrum, following the method of Giacalone & Jokipii (1999) and constructed as a sum of finite number of randomly oriented plane waves. Wavenumbers were evenly distributed in logarithmic scale between k_{min} and k_{max} . The number of modes was set to 500 and $(k_{max}/k_{min}) = 100$. The exact value of k_{max} depends on magnetic field strength and is determined from (1) and (2) to properly fit the correlation length. We have checked that in the small scattering regime we obtain the theoretically expected result from the random walk process with a correlation length equal to λ_B .

Figure 4 shows the result of the calculation of the extended emission pattern at different energies for a range of IGMF strengths. The extended emission signal appears on top of the point-source signal and of the residual charged cosmic-ray background. The difficulties of detection of the extended emission are evident from the figure. The extended source signal is always subdominant. The point-source signal dominates in the $0^\circ < \theta < 0.17^\circ$ angular range, while the residual cosmic-ray background dominates outside $\theta_c = \sqrt{0.03} \simeq 0.17^\circ$.

Figure 5, which is a direct analog of the analytical estimate in Figure 2, provides a further illustration of the dominance of the point-source flux. The extended source spectrum is split into two components, outside and inside θ_c . In the $B \sim 10^{-12}$ G case, the extended source flux is largely dominated by the component inside θ_c (and hence, within the extent of the primary source point-spread function). If $B \sim 10^{-11}$ G, emission flux outside θ_c is just a factor of 2 below the flux within θ_c . Given the overall weakness of the extended emission

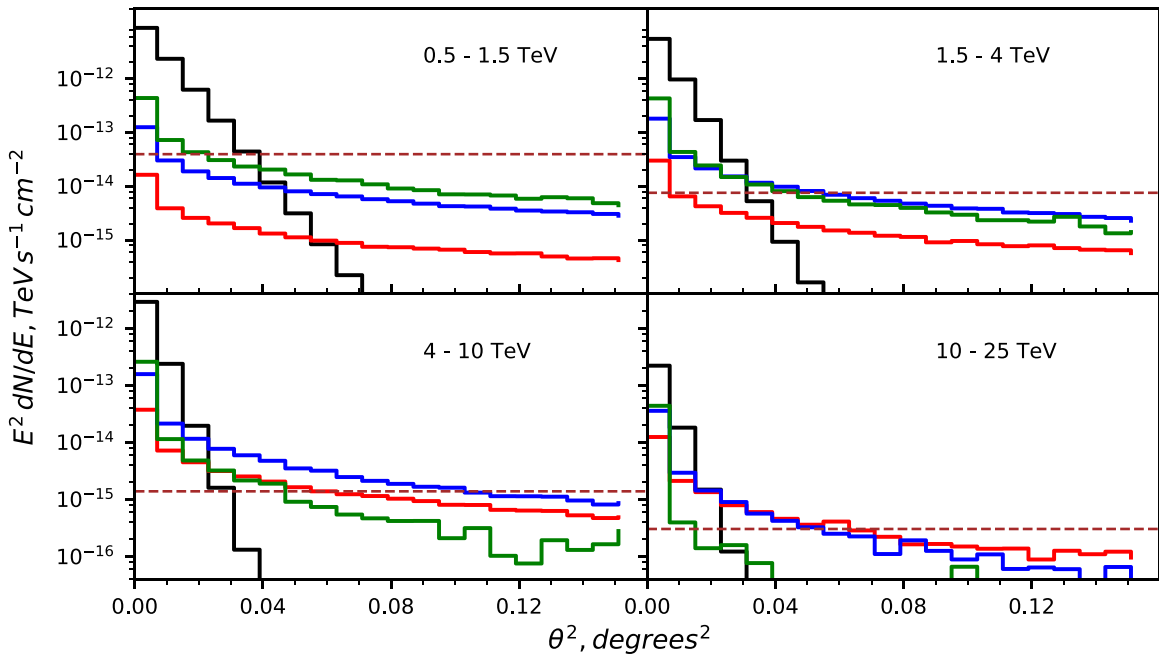


Figure 4. Angular distribution of primary and secondary photons in different energy ranges. Black histograms show the primary point-source signal; green, blue, and red histograms show the extended emission calculated for different magnetic field strengths: 10^{-12} G, 3×10^{-12} G, and 10^{-11} G. Horizontal dashed line shows the level of residual cosmic-ray electron background measured by HESS (Kerszberg et al. 2017).

signal in the case of a strong field, it is thus reasonable to use the combination of regions $\theta < \theta_c$ and $\theta > \theta_c$, searching for the deviations from the PSF of the instrument in the angular range $[0^\circ; 0^\circ.4]$.

Figure 5 also illustrates the effect of the overall suppression of the extended source flux below E_{crit} (10) in the strong IGMF case. This is most clearly seen in the right panel of the figure. In this case $E_{\text{crit}} = 8$ TeV for the assumed jet opening angle. Comparing the extended source flux above 10 TeV for the $B = 10^{-11}$ G case with that for the $B = 10^{-12}$ G case (shown in the left panel) cone can see that the total extended source fluxes are comparable above 10 TeV. This is not the case for the 1 TeV band fluxes. The opening angle of the secondary emission cone at 1 TeV in the case of the $B \sim 10^{-11}$ G field is wider than the jet opening angle and the flux is suppressed by a factor of 10.

5. Results and Discussion

We have used the results of the Monte Carlo modeling to investigate the detectability of the extended emission signal with CTA. To do this, we have calculated the statistics of the point-source signal, extended emission signal, and residual cosmic-ray background in each angular bin of the histograms shown in Figure 4, for different CTA exposures. In this way we have generated mock CTA data sets. We have fitted the mock data with a model of point source plus the residual cosmic-ray background model, ignoring the presence of the extended source. We have then estimated the significance of detection of the extended emission in the simulated data set by calculating the level of inconsistency of the “point source + residual cosmic ray electron background (Kerszberg et al. 2017)” model with the simulated data.

The results of this analysis are shown in Figure 6. If the IGMF strength is below 3×10^{-12} G, the extended signal is detectable with a significance larger than 3σ in the energy ranges 0.5–1.5 TeV and 1.5–4 TeV. A somewhat stronger

magnetic field, $3 \times 10^{-12} < B < 6 \times 10^{-12}$ G, is still marginally detectable through the extended emission at somewhat higher energy, up to 10 TeV. The extended emission signal associated with the 10^{-11} G IGMF is not detectable in a 50 hr exposure.

Figure 7 shows the exposure needed for the 3σ evidence for and 5σ discovery of the extended emission for different IGMF strengths. From this figure one can see that with a 150 hr exposure, evidence for the presence of extended emission in the 10 TeV energy range can be found even for the magnetic field with the strength of 10^{-11} G. Extended emission shaped by deflections of electrons and positrons in such IGMF can be discovered in such a very long exposure, $T \simeq 400$ hr.

CTA is a unique instrument that will be capable of detecting the extended emission in the multi-TeV energy range. Next generation air shower arrays, the Large High Altitude Air Shower Observatory (LHAASO; Bai et al. 2019), the Southern Wide-field Gamma-ray Observatory (SWG0; Albert et al. 2019), and Tunka Advanced Instrument for cosmic rays and Gamma Astronomy (TAIGA; Budnev et al. 2020) do not achieve a comparable level of suppression of charged cosmic-ray background in the energy range below 10 TeV and have much worse angular resolution in this energy range. Both factors strongly reduce sensitivity for the extended emission search.

Mrk 501 is the brightest extragalactic source in the 10 TeV energy range. Its uniqueness can justify such an ultra-deep exposure (perhaps accumulated over several years of observations). It can serve not only for the measurement of the IGMF but also for the study of the high-energy end of blazar spectra and for the precision measurements of the EBL.

Optimization of CTA performance for the search of extended emission around Mrk 501 will build upon previous developments with the current generation Cerenkov telescopes. Recent measurements of extension of the Crab Nebula show the potential of such a search (Holler et al. 2018). Mrk 421 and

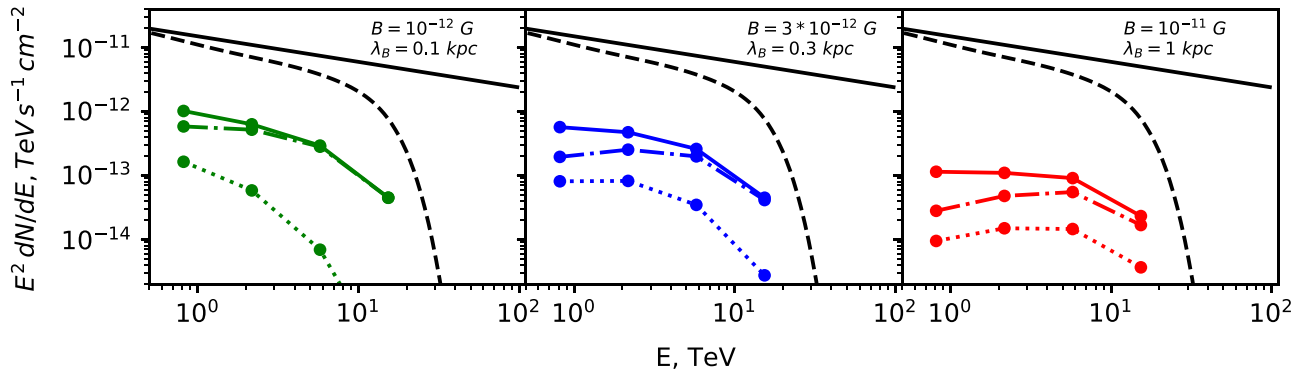


Figure 5. Intrinsic spectrum of Mrk 501 (black solid line) in comparison with the absorbed spectrum (black dashed line) and the spectrum of secondary emission (colored lines) for different parameters of the magnetic field. Solid colored line corresponds to the total flux of the secondary emission from the source, while dashed-dotted and dotted lines are the fluxes in the angular ranges $[0; \theta_c]$ and $[\theta_c; 0.4]$ degrees.

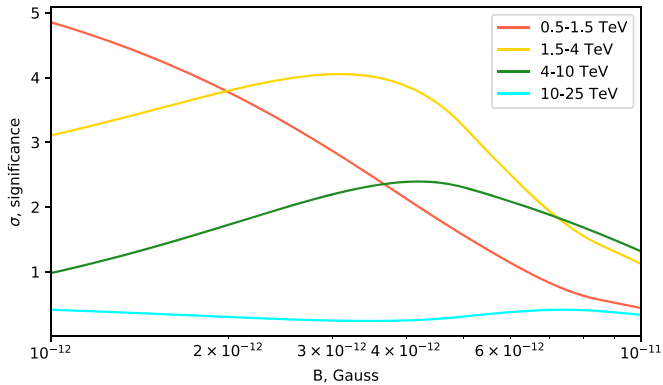


Figure 6. Significance of detection of the extended emission signal in different energy ranges as a function of the assumed magnetic field strength. The assumed exposure of CTA is $T = 50$ hr.

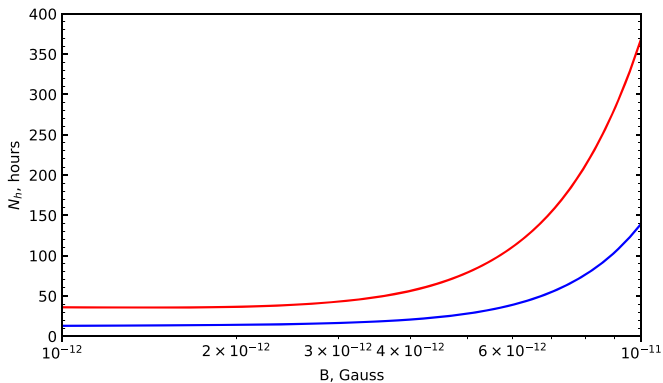


Figure 7. CTA exposure time needed for 3σ (lower curve) and 5σ (upper curve) detection of the extended emission signal, as a function of IGMF strength.

Mrk 501, two sources with TeV band fluxes comparable to Crab have already been subjects of extended emission searches with MAGIC. Aleksić et al. (2010) have derived constraints on the extended emission flux at the level of 5% of the Crab Nebula. HESS has derived a tight constraint of $30''$ on the angular size of the source generating the bulk of Mrk 421 flux. The source emission in this angular range is dominated by primary photons rather than by the cascade emission.

To summarize, we have shown that direct detection of the strong cosmological magnetic field, which is needed for the resolution of the tension between different measurements of the Hubble parameter (Jedamzik & Pogosian 2020) and for the

explanation of the EDGES 21 cm line opacity (Natwariya & Bhatt 2020) is possible with the γ -ray measurement technique. At least one source, Mrk 501, is suitable for this purpose. A search for the extended emission around Mrk 501 in the 1–10 TeV energy range can result in the detection of IGMF with a strength of up to 10^{-11} G and a correlation length of up to 10 kpc.

We thank Guilhem Lavaux and Jens Jasche for providing the constrained simulations of the Local Universe derived using the BORG algorithm. We also thank Karsten Jedamzik and Levon Pogosyan for clarifying the details of the estimate of cosmological magnetic field from their analysis of the CMB data.

This work has been supported by the French National Research Agency (ANR) grant ANR-19-CE31-0020 and Russian Science Foundation grant 20-42-09010.

ORCID iDs

Andrii Neronov  <https://orcid.org/0000-0002-6748-368X>

References

- Ackermann, M., Ajello, M., Baldini, L., et al. 2018, *ApJS*, **237**, 32
 Albert, A., Alfaro, R., Ashkar, H., et al. 2019, arXiv:1902.08429
 Aleksić, J., Antonelli, L. A., Antoranz, P., et al. 2010, *A&A*, **524**, A77
 Bai, X., Bi, B. Y., Bi, X. J., et al. 2019, arXiv:1905.02773
 Banerjee, R., & Jedamzik, K. 2004, *PhRvD*, **70**, 123003
 Berezhinsky, V., & Kalashev, O. 2016, *PhRvD*, **94**, 023007
 Bowman, J. D., Rogers, A. E. E., Monsalve, R. A., Mozdzen, T. J., & Mahesh, N. 2018, *Nature*, **555**, 67
 Budnev, N., Astapov, I., Bezyazeev, P., et al. 2020, *JInst*, **15**, C09031
 Coutiño de Leon, S., Alonso, A. C., Rosa-Gonzalez, D., & Longinotti, A. L. 2019, ICRC (Madison, WI), **36**, 654
 Durrer, R., & Neronov, A. 2013, *A&ARv*, **21**, 62
 Fujita, T., & Kamada, K. 2016, *PhRvD*, **93**, 083520
 Giacalone, J., & Jokipii, J. R. 1999, *ApJ*, **520**, 204
 Gilmore, R. C., Somerville, R. S., Primack, J. R., & Dominguez, A. 2012, *MNRAS*, **422**, 3189
 Giovannini, M., & Shaposhnikov, M. E. 1998, *PhRvD*, **57**, 2186
 Giroletti, M., Giovannini, G., Cotton, W. D., et al. 2008, *A&A*, **488**, 905
 Holler, M., Berge, D., Hahn, J., Khangulyan, D., & Parsons, R. D. 2018, ICRC (Busan), **301**, 676
 Jasche, J., & Lavaux, G. 2019, *A&A*, **625**, A64
 Jasche, J., & Wandelt, B. D. 2013, *MNRAS*, **432**, 894
 Jedamzik, K., & Pogosian, L. 2020, *PhRvL*, **125**, 181302
 Jedamzik, K., & Saveliev, A. 2019, *PhRvL*, **123**, 021301
 Kachelriess, M., Ostapchenko, S., & Tomas, R. 2012, *CoPhC*, **183**, 1036
 Kalashev, O., & Kido, E. 2015, *JETP*, **120**, 790

- Kerszberg, D., Kraus, M., Kolitzus, D., et al. 2017, ICRC (Busan), 35, 215,
[https://indico.snu.ac.kr/indico/event/15/session/5/contribution/694/
material/slides/0.pdf](https://indico.snu.ac.kr/indico/event/15/session/5/contribution/694/material/slides/0.pdf)
- Kronberg, P. P. 1994, *RPPh*, 57, 325
- Lavaux, G., & Hudson, M. J. 2011, *MNRAS*, 416, 2840
- Marinacci, F., Vogelsberger, M., Pakmor, R., et al. 2018, *MNRAS*, 480, 5113
- Natwariya, P. K., & Bhatt, J. R. 2020, *MNRAS*, 497, L35
- Neronov, A., & Semikoz, D. V. 2009, *PhRvD*, 80, 123012
- Neronov, A., & Vovk, I. 2010, *Sci*, 328, 73
- Planck Collaboration 2016, *A&A*, 596, A103
- Planck Collaboration, Aghanim, N., & Akrami, Y. 2020, *A&A*, 641, A6
- Riess, A. G., Casertano, S., Yuan, W., Macri, L. M., & Scolnic, D. 2019, *ApJ*,
876, 85
- Taylor, A., Vovk, I., & Neronov, A. 2011, *A&A*, 529, A144
- Wong, K. C., Suyu, S. H., Chen, G. C.-F., et al. 2020, *MNRAS*, 498, 1420